Theoretical Study of Catalytic Activity Modifications in CO$_2$ Methanation Induced by an Electric Field in Solid-Oxide Cells

ARTICLE

Theoretical Study of Catalytic Activity Modifications in CO_2 Methanation Induced by an Electric Field in Solid-Oxide Cells

Katsuhiro Wakamatsu,*[a,b] Takaaki Yasuda,[a] Masato Aratani [b] and Teppei Ogura *[a,b]

Non-faradaic electrochemical modification of catalytic activity (NEMCA) by the induction of an external electric field can improve catalyst performance. Previous reports individually investigated the effects of direct electric-field induction or co-adsorbed oxygen atoms for each as the possible activation factor of the NEMCA mechanism. We investigated the mechanism of NEMCA in CO_2 methanation in a solid-oxide cell (SOC) using density functional theory (DFT). DFT calculations were performed for the hydrocarbon species on Ni (111) with a directly applied electric field and co-adsorbed oxygen atoms, and we compared them to clarify which effect is the dominant factor in the NEMCA mechanism over CO_2 methanation based on practical SOC system conditions. The rate-determining steps (RDSs) of CO_2 methanation were discussed based on detailed kinetic simulations. We found that the direct effects of the electric field on surface adsorption differed for each intermediate and that all RDSs accelerated with the application of the electric field. As the number of co-adsorbed oxygen atoms increased, all intermediates adsorbed less strongly on the surface, CHO and CO_2 dissociations decelerated, and CH_4 desorption accelerated. The effect of the co-adsorbed oxygen atoms on the kinetic energy is larger than that of direct electric field induction. Detailed kinetic simulations revealed that overall CO_2 methanation accelerates in solid-oxide electrolysis cell mode (with decreasing oxygen coverage).

Introduction

Currently, countries worldwide face severe energy issues, including the exhaustion of fossil fuels. As part of the concerted efforts to fight against climate change, governments are required to reduce greenhouse gases such as carbon dioxide through international treaties. Hence, the expansion of renewable energy sources is crucial. Hydrogen gas and methane are expected to be important energy carriers. Hydrogen gas can be formed by water electrolysis using renewable energy sources; however, its transport and storage presents some problems. In contrast, methane can be used in the existing infrastructure and has a high hydrogen weight density, making it important to develop a method for converting hydrogen into methane. To accomplish this, we performed CO_2 methanation[1–10] using a Ni-metal catalyst in a solid-oxide cell (SOC), which is effective for carbon dioxide capture and storage.

CO_2 methanation:

$$CO_2 + 4H_2 \rightarrow CH_4 + 2H_2O, \Delta_r H^0_{298K}= -165 \text{ kJ/mol} \quad [1]$$
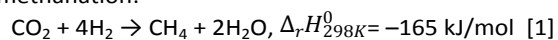
CO_2 methanation is an exothermic and volume-decreasing reaction; therefore, high CO_2 conversion is observed under low-temperature and high-pressure conditions.[10] However, the reaction rate is low under low-temperature conditions. To solve this problem, non-faradaic electrochemical modification of catalytic activity (NEMCA) using an external electric field, also called electrochemical promotion of catalysis (EPOC), has attracted attention in recent years.[11–21]

NEMCA can promote catalytic reactions at low temperature[22,23] and was proposed first in 1981 for ethylene and propylene epoxidation on Ag catalysts at ≈400 °C and atmospheric pressure[24]. In early experimental studies[24–38], the NEMCA effect has been demonstrated in many reaction systems; it is not limited to specific solid electrolytes, catalysts, or pure catalytic films. For example, CO + O_2 / Pt / YSZ[33] and C_2H_4 + O_2 / Pt / YSZ[34] have been studied as metal (Me) / YSZ systems, and some NO reducing reactions[35] have been studied as Me / β'' –Al_2O_3 systems. The NEMCA effect has also been observed when a dispersed catalyst or a metal oxide catalyst was used[31,32]. The electrochemically induced spillover of ionic species (spillover oxygen atoms), including alkali species on the metal electrode surface, has been proposed as an NEMCA mechanism.[25,26,29,30] It is assumed that the oxygen back-spillover species $(O^{\delta-} - \delta^+)$ increases the rate and selectivity of catalytic reactions. An oxygen back-spillover species from the solid-oxide electrolyte to electrode surface has been proposed, which should be highly polar, bonded more strongly to the metal surface than chemisorbed oxygens, and less reactive than chemisorbed oxygens.[12] To observe the spillover of the oxygen species, X-ray photoelectron spectroscopy (XPS)[36], temperature

[a.] Department of Nanotechnology for Sustainable Energy, Graduate School of Science and Technology, Kwansei Gakuin University, 1 Gakuen Uegahara, Sanda, Hyogo, 669-1330, Japan.

[b.] Department of Physics, Graduate School of Science and Technology, Kwansei Gakuin University, 1 Gakuen Uegahara, Sanda, Hyogo, 669-1330, Japan.

*Corresponding author e-mail addresses: (K.W.) katsu29yukke@gmail.com, (T.O.) t-ogura@kwansei.ac.jp

Electronic Supplementary Information (ESI) available. See DOI: 10.1039/x0xx00000x

programmed desorption (TPD),[37] and cyclic voltammetry (CV)[38] studies have been conducted. For instance, an XPS experiment involving a porous Pt electrode under ultrahigh vacuum (UHV) revealed a peak at 528.8 eV in addition to peaks at 530.4 eV, which are characteristic of adsorbed oxygen atoms when electrochemical pumping of the voltage is performed between the reference and working electrodes (V_{WR} = 1.2 V). It was assumed that this peak at 528.8 eV corresponds to a spillover oxygen atom.[36]

Several theoretical studies on spillover species have been performed for catalytic reactions on metal catalyst surfaces.[39–48] For example, Vayenas and Pitselis developed a steady-state one-dimensional surface reaction and diffusion model to simulate the NEMCA effect of a porous catalyst on a solid electrolyte.[45] Leiva et al. studied the structural and energetic properties of Na/Pt (111) and O/Pt (111) using quantum mechanical calculations and Monte Carlo (MC) grand canonical simulations to understand the NEMCA effect[39]. Fragkopoulos et al. developed a macroscopic multidimensional kinetic model for CO oxidation that considered the oxygen spillover species and evaluated the CO_2 production rate using NEMCA.[40,41,48] In addition, Liu et al. performed first-principles calculations of the oxygen-coverage effect for hydrogen oxidation on Ni (111) facets and found that the binding energy of H, O, and OH species on the Ni surface decreases as the co-adsorbed oxygen-atom coverage increases owing to the change in the Ni atomic charge by the co-adsorbed oxygen atoms. They reported that the binding energy of H_2O on the Ni surface increased as the co-adsorbed oxygen-atom coverage increased as a result of the increase in the positive species charge and hydrogen bonds between H_2O and the co-adsorbed oxygen atoms.[42] However, the existence of spillover oxygen atoms has not yet been confirmed, and the connection between spillover and the change in catalytic activity and selectivity is unclear; therefore, the theoretical concepts and mechanistic models are not sufficiently clear to explain the NEMCA effect. In addition, the electric field directly changed the electrostatic state of the catalyst but this effect has not been studied in detail.

Several experimental and theoretical studies have been performed on the direct electric field effect.[22,23,49–59] For instance, Sekine et al. conducted an experiment on catalytic steam methane reforming (SMR) at low temperatures under an electric field and reported that the process is considerably promoted under an electric field.[22,23] Wang and Liu performed first-principles calculations to evaluate the direct electric-field effect of S atoms related to H_2S dissociation on Ni (100) and (111). They reported that the adsorption energy of S atoms changes slightly in both Ni facets because the Fermi level of the Ni metal surface is shifted by the direct electric field.[50] In addition, Che et al. calculated the adsorption of CH_x species and co-adsorption of methyl species on the Ni (111) and (211) surfaces in the presence of an external electric field using first-principles calculations. They reported that the adsorption energies of H atoms, C atoms, and CH, CH_2, and CH_3 species on both Ni facets were altered by the electric field. They also reported that the adsorbates adsorb more strongly on the Ni (211) surface than on the Ni (111) surface and that the different

adsorption sites on the Ni (211) surface have different local electric field distributions.[52,53]

As mentioned above, although the individual effects of the electric field or co-adsorbed oxygen have been investigated, the detailed activation mechanism of NEMCA has not been elucidated. In this study, we computationally evaluated both effects of a direct electric field and co-adsorbed oxygen atoms on catalytic activation to reveal the activation mechanism of NEMCA because it is difficult to individually probe these effects experimentally. In other words, we investigated the effects induced by a direct electric field and co-adsorbed oxygen and compared them to clarify which effect is dominant. First, we performed detailed kinetic simulations of CO_2 methanation on a Ni surface and identified the reaction paths. We determined the rate-determining steps (RDSs) of CO_2 methanation on the Ni surface using sensitivity analysis. We then theoretically investigated the effect of direct electric-field induction using first-principles calculations. We calculated the adsorption and surface reaction energies of hydrocarbon-species-related RDSs during CO_2 methanation on the Ni (111) facet using our elementary-step mechanism with a direct electric field. Our density functional theory (DFT) calculations focused on only the Ni (111) facet owing to the structural complexity of the Ni (211) facet. We evaluated the promotional or restraint effect of the RDSs toward overall CO_2 methanation by performing detailed kinetic simulations. Subsequently, we theoretically investigated the effect of oxygen co-adsorption in the same manner as the direct electric field induction and evaluated the promotional or restraint effect of RDSs toward the overall CO_2 methanation through a detailed kinetic simulation using the activation energy. Finally, based on the knowledge of the kinetic mechanism, we discuss the enhancement of the catalytic activity by the direct effect of electric-field induction and the effect of oxygen co-adsorption, identifying the main factor in the NEMCA mechanism for CO_2 methanation.

Numerical methods

DFT computational details

In our work, the improvements in catalytic activity upon application of an electric field were computationally investigated using DFT calculations.[60,61] Seven hydrocarbon species (H, O, CH, CO, CH_3, CO_2, and CHO) were related to the three RDSs as reaction intermediates in CO_2 methanation. For simplicity, these hydrocarbon species were assumed to be adsorbed on the Ni (111) facets as reaction intermediates in CO_2 methanation. The definitions of the direct electric field induction and oxygen-coverage conditions on the Ni (211) facet and their behaviors are complex. Therefore, DFT calculations were performed only for the Ni (111) facet to easily estimate the direct electric field and co-adsorption effects. Ni is a well-known metal catalyst used in SOCs. For repeated slab models,[62] a three-layer slab of Ni (111) with a 3×3 unit cell (or 3×2 and 2×2 unit cells for co-adsorbed oxygen atom surface models in which ϑ = 1/6 and 1/4, respectively) was used to evaluate the surface reaction; the width of the vacuum layer was set to 10 Å. Here,

the Ni lattice parameter is 3.518 Å, which is in good agreement with the experimental value of 3.52 Å.[63] DFT calculations were performed using the Cambridge Sequential Total Energy Package (CASTEP) with a plane-wave basis set.[62] The Perdew (Burke) Ernzerhof exchange-correlation functional[64] was applied with dimensions of 1×1×1 and 4×4×1 for all gaseous species and others as Monk–Horst–Pack k-points[65], respectively. Note that Monk–Horst–Pack k-points with dimensions of 4×6×1 and 6×6×1 were used for co-adsorbed oxygen atom surface models with ϑ = 1/6 and 1/4, respectively, to align the width of the reciprocal lattice space to the models with other oxygen coverage. The cutoff energies of a plane wave were 450 eV and 630 eV (for the S- and O-containing species with an electric field and all species with co-adsorbed oxygen atoms). In all the systems, the calculation of gas-phase species did not consider the application of an electric field. In addition, OTFG ultrasoft pseudopotentials were used,[62] and spin-polarization was considered in our calculations because Ni metal is a ferromagnetic substance. In transition state (TS) searches, linear synchronous transit (LST) and quadratic synchronous transit (QST) methods were utilized.[66,67] The strength of species adsorption was calculated using the adsorption energy, defined as follows:

$$E_{ads} = E_{M/slab} - (E_M + E_{slab}) \ [2]$$

where E_{ads} is the adsorption energy, $E_{M/slab}$ is the total energy of the surface metal slab with the adsorbed species on the metal surface, E_M is the total energy of the free atoms or molecules, and E_{slab} is the total energy of the surface metal slab alone. The reaction energies of dissociation, AB* + * → A* + B*, and associative desorption, A* + B* → AB + 2*, are defined in Eq. 3 and 4, respectively:

$$E_{rxn,dis} = (E_{A/slab} + E_{B/slab}) - (E_{AB/slab} + E_{slab}) \ [3]$$

$$E_{rxn,ass} = (E_{AB} + 2E_{slab}) - (E_{A/slab} + E_{B/slab}) \ [4]$$

where E_{rxn} denotes the reaction energy; $E_{A/slab}$, $E_{B/slab}$, and $E_{AB/slab}$ are the total energies of the surface metal slab with adsorbed species A, B, and AB on the metal surface, respectively; and E_{AB} is the total energy of the free molecule, AB. The activation energy is defined as follows:

$$E_{act} = E_{TS} - E_{reactants} \ [5]$$

where E_{act} is the activation energy, E_{TS} is the total energy of the transition states, and $E_{reactants}$ is the sum of the total energies of the reactants.

Thin-film condenser model

The thin-film condenser model shown in Fig. 1 was used to evaluate the direct effect of the electric field. In this model, the slab is sandwiched between two condenser boards connected to the outlet electrode. The electric field was applied in two directions perpendicular to the Ni surface, and its magnitude

was set to 0, ±0.25, or ± 0.5 V/Å. The positive and negative electric field values represent the [0 0 1] (from the Ni-metal surface to the gas phase) and [0 0 –1] (from the gas phase to Ni metal surface) perpendicular directions, respectively. In addition, the adsorption sites of the hydrocarbon species on Ni (111) were set to the most stable surface sites of each hydrocarbon species, as previously determined by the Ogura group and early studies that applied direct electric field calculations (H atom: fcc,[42,52,68–71] O atom: fcc,[27,42,43,68–71] CH: fcc,[52] CO: hcp,[70–72] CH₃: fcc,[52,71] CO₂: top,[70] CHO: hcp[71]). The adsorption sites of the hydrocarbon species on the Ni (111) surface are shown in Fig. 2. The fcc and hcp sites are hollow sites on the 3rd and 2nd Ni atom layers, respectively. The top site was the Ni atom of the upper (1st) Ni atom layer. The energy changes (adsorption or reaction energies) induced by varying the electric field are defined as follows:

$$\Delta E_{EF} = E_{with\ EF} - E_{without\ EF} \ [6]$$

where ΔE_{EF} is the relative value based on the adsorption or reaction energy without an electric field, $E_{with\ EF}$ is the adsorption or reaction energy with an electric field, and $E_{without\ EF}$ is the adsorption or reaction energy without an electric field.
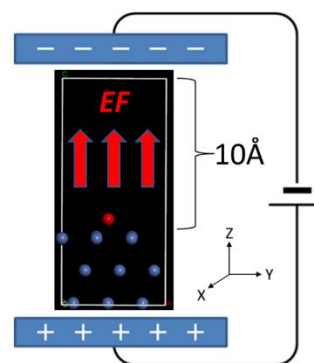

Fig. 1 Schematic of the thin-film condenser model with the electric field in the [0 0 1] direction.
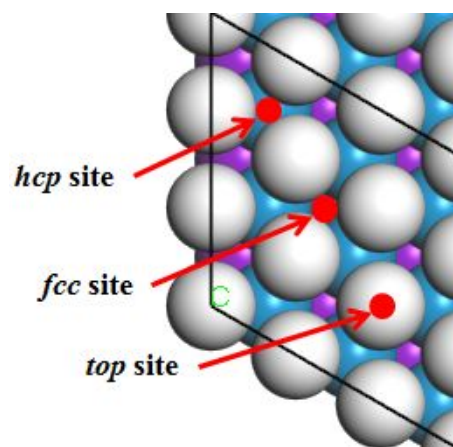

Fig. 2 Adsorption sites of hydrocarbon species on the Ni (111) surface (white, blue, and violet balls denote the 1st, 2nd, and 3rd Ni-layer atoms, respectively).

Co-adsorbed oxygen atom surface model

Meanwhile, to evaluate the effect of co-adsorbed oxygen atoms, the co-adsorbed oxygen atom surface model, a Ni (111) surface slab model with varying numbers of oxygen atoms, was assumed, as shown in Fig. 3. The oxygen-atom coverage was set to ϑ = 0, 1/9, 1/6, 2/9, 1/4 or 3/9. Co-adsorbed oxygen atoms were set at all *fcc* sites on the Ni (111) facet because the most stable surface site of the oxygen atom is the *fcc* site. The adsorption sites of the hydrocarbon species on Ni (111) were set as *fcc* sites. The most stable surface site for some hydrocarbon species on the pure Ni surface was not the *fcc* site; however, if co-adsorbed oxygen atoms exist at an *fcc* site on the Ni surface, all hydrocarbon species are the most stable on the *fcc* site of Ni (111) owing to the steric barrier effect caused by the existence of co-adsorbed oxygen atoms on another *fcc* site. Here, hydrocarbon species were set to the *hcp* site only in the case of ϑ = 1/4 owing to space restriction in the slab model structure with 2×2 unit cells; only CH$_3$ moves from a *fcc* site to a *hcp* site after geometry optimization when ϑ = 1/6. The energy changes (adsorption or reaction energy) with the co-adsorbed oxygen atoms are defined as follows:

$$\Delta E_{co-ad\,O} = E_{with\,co-ad\,O} - E_{without\,co-ad\,O} \quad [7]$$

where $\Delta E_{co-ad\,O}$ is the relative value based on the adsorption or reaction energy without co-adsorbed oxygen atoms, $E_{with\,co-ad\,O}$ is the adsorption or reaction energy with co-adsorbed oxygen atoms, and $E_{without\,co-ad\,O}$ is the adsorption or reaction energy without co-adsorbed oxygen atoms. Notably, the co-adsorbed oxygen-atom surface models ϑ = 1/6 and 1/4 were compared with ϑ = 0 in the cases of 3×2 and 2×2 unit cells, respectively.
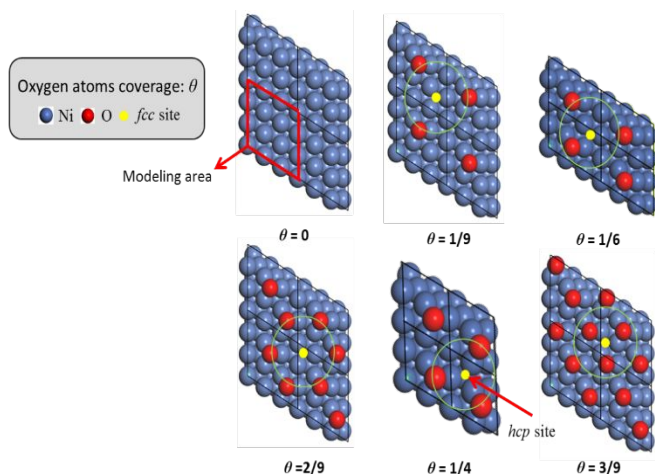

Fig. 3 Schematic of the co-adsorbed oxygen-atom surface model.

Detailed kinetic simulation

To calculate the promotional or restraint effect of the overall CO$_2$ methanation, we used a single continuously stirred tank reactor (CSTR) model (Fig. 4). We set the number of reactors to $N = 1$ in a multi continuously stirred tank reactor (multi-CSTR) model using the ODE15s solver in MATLAB for detailed kinetic simulation. Note that this model assumes that the gas composition is mixed perfectly in the reactor and ignores surface diffusion.[71,73–77]
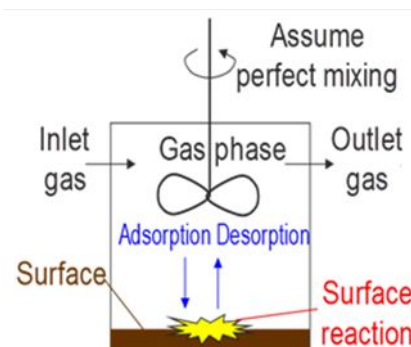

Fig. 4 Schematic of the CSTR model.

ODE15s is a variable-order solver based on numerical differentiation formulas for solving differential algebraic problems[78,79]. The equation of mass conversion that can be solved for the time-derivative molar number of the ith species n_i is as follows[71,73–77]:

$$\frac{dn_i}{dt} = A_s \sum_{j=1}^{N_{rxn}} v_{j,i} \left[k_j \prod_{i=1}^{S_R} C_i^{-v_{j,i}} - k_{-j} \prod_{i-1}^{S_P} C_i^{v_{j,i}} \right] + \gamma_i \left(F_{i,in} - \frac{VC_i}{t_{res}} \right) \quad [8]$$

where A_s is the catalyst surface area; N_{rxn} is the reaction number; $v_{j,i}$ is the stoichiometric ratio of the ith species in the jth reaction; k_j and k_{-j} are the forward and reverse rate constants in the jth reaction, respectively; S_R and S_P are the numbers of reactants and products in each reaction, respectively; C_i is the ith species concentration; $F_{i,in}$ is the inlet flow amount of the ith species; V is the reactor volume; and t_{res} is the residence time. Note that if the gas and surface species are considered, the switching parameter γ_i is 1 and 0, respectively. $F_{i,in}$ is defined as follows:

$$F_{i,in} = \left(\frac{PV}{RT} \right) \left(\frac{y_{i,in}}{t_{res}} \right) \quad [9]$$

where P and T are the pressure and temperature of the reactor, respectively, and $y_{i,in}$ is the mole fraction of species i in the feed. Moreover, k_j is defined using the Arrhenius equation as follows:

$$k_j = A_j T^{\beta_j} \exp\left(-\frac{E_{a,j}}{RT} \right) \quad [10]$$

where A_j is the frequency factor (pre-exponential factor) in the jth reaction, β_j is the temperature exponent in the jth reaction, R is the ideal-gas constant (8.3145 J/mol·K), and $E_{a,j}$ is the activation energy for the jth reaction. In our simulation, β_j in the molecular adsorption is –0.5 owing to the barrierless reaction, and the β_j values for the dissociative adsorption and the surface reaction are 0. The reverse rate constants were calculated from the corresponding forward rate constants using the equilibrium constants, as follows:

$$k_{-j} = k_j \exp\left(\frac{\Delta G_j}{RT}\right) \text{ [11]}$$

where ΔG_j is the Gibbs free energy in the jth reaction and is expressed as follows:

$$\Delta G_j = \Delta H_j - T\Delta S_j \text{ [12]}$$

In Eq. 12, ΔH_j is the enthalpy for the jth reaction, and ΔS_j is the entropy for the jth reaction. More detailed theoretical information is provided by Blaylock et al.[71,73] We recreated the kinetic simulation conditions of the experiment reported by Atsumi et al.[2] The inflow composition was $H_2:CO_2$ = 4:1 (total inflow rate of 25 mL/min), and the electrolyte thickness and diameter were assumed to be 500 µm and 20 mm, respectively, so that reactor volume was 1.57×10^{-7} m³. The surface area of the catalyst was determined by parameter fitting and was in agreement with the experimental results. The operating temperature was assumed to be 673 K because the faradaic efficiency of CO_2 methanation with NEMCA was the highest at 673 K, according to their report. In addition, the Ni particle diameter was assumed to be 7 nm, and the surface ratio was determined to be (111)*: (211)*: (100)* = 0.74:0.11:0.15 based on the Wulff theorem.[73,80] Elementary steps in CO_2 methanation were selected from the data reported by Blaylock et al. based on quantum calculations,[71,73] and kinetic and thermodynamic parameters were adjusted to agree with the experimental results reported by Atsumi et al. Our simulation conditions, assuming elementary steps in CO_2 methanation, as well as the kinetic and thermodynamic parameters, are listed in Table 1, S2, and S3, respectively.

Table 1 Simulation conditions.

Parameters	Value
Pressure [Pa]	101325
Reactor volume [m³]	1.57×10^{-7}
Temparature [K]	673
Catalyst surface area [m²]	2.32×10^{-3}
Number of sites per surface area [sites/Å²]	0.18639
Simulation time [s]	1000
Inflow composition (total amounts is 25 [ml/min])	$H_2 : CO_2$ = 4: 1

In the sensitivity analysis in this study, we multiplied the rate constant k of each elementary step (the pre-exponential factor A) by 1.1 to calculate the selectivity for each gas-generation rate (CH_4, CO, and H_2O), In other words, we calculated the difference

between the generated species concentrations in the case of A multiplied by 1.1 and 1 (original conditions). The sensitivity coefficients were obtained as follows:

$$S_{ij} = \frac{(N_{i,k_j \times 1.1} - N_{i,k_j})/N_{i,k_j}}{\Delta k_j / k_j} = \frac{(N_{i,k_j \times 1.1} - N_{i,k_j})/N_{i,k_j}}{0.1} \text{ [13]}$$

where S_{ij} is the sensitivity coefficient of the ith species (CH_4, CO, or H_2O) in the jth reaction (Reaction 1–101), k_j is the rate constant for the jth reaction, Δk_j is ($1.1k_j - k_j$), $N_{i,kj}$ is the concentration of the ith species in the case of k_j (original conditions), and $N_{i,k_j \times 1.1}$ is the concentration of the ith species in the case of $k_j \times 1.1$.

Results and discussion

Identifications of RDSs in CO_2 methanation

First, we attempted to clarify the mainstream reaction paths (dominant elementary steps) of CO_2 methanation on the Ni surface using sensitivity analysis and detailed kinetic simulations to investigate and compare the effects of direct electric field induction and oxygen atom co-adsorption.

We performed a sensitivity analysis of the CO_2 methanation reaction paths to identify the RDSs of the CO_2 methanation on the Ni surface. In our simulation results, the sensitivity of the elementary steps of CO_2 methanation to the gas-generation rate was highest for Ni (211). The results of the sensitivity analysis of the CO_2 methanation reaction paths for Ni (211) are shown in Fig. 5.
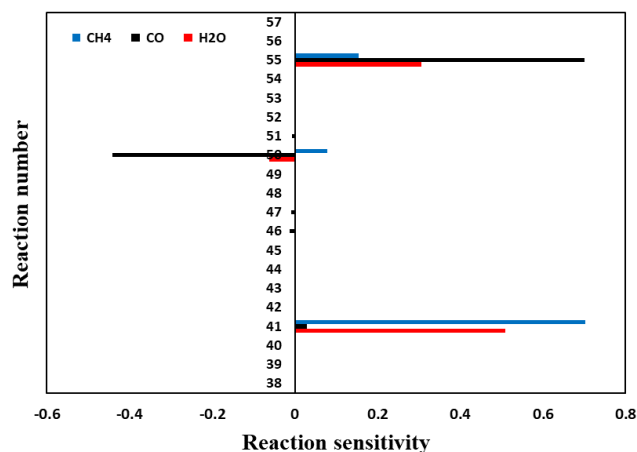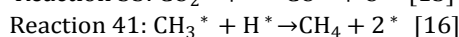

Fig. 5 Sensitivity of elementary steps of CO_2 methanation on Ni (211) to gas-generation rate.

They revealed that the RDSs for the CO_2 methanation on Ni (211) involved three reactions: CHO* dissociation (reaction 50), CO_2* dissociation (reaction 55), and CH_4 desorption (reaction 41).

RDSs for CO_2 methanation:

Reaction 50: $CHO^* + {}^* \rightarrow CH^* + O^*$ [14]
Reaction 55: $CO_2{}^* + {}^* \rightarrow CO^* + O^*$ [15]
Reaction 41: $CH_3{}^* + H^* \rightarrow CH_4 + 2{}^*$ [16]
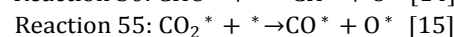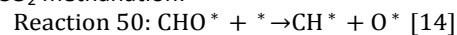
where [chemical species]* and * represent a chemical species adsorbed on the catalytic surface and a vacant site on the catalytic surface, respectively. In addition, detailed kinetic simulations of CO_2 methanation on the Ni surface were conducted to identify the main reaction pathways. Fig. 6 shows a schematic of CO_2 methanation on Ni (211). CO_2 in the gas phase was adsorbed on the Ni surface, and one C–O bond in CO_2^* was dissociated. Subsequently, CO* reacts with H* to generate CHO*, then another C–O bond in CHO* is dissociated. Finally, CH* reacts with H* atoms to generate CH_4, which is desorbed into the gas phase. The reaction mechanism and RDSs for CO_2 methanation on Ni (111) were the same as those on Ni (211), although the sensitivity of the elementary steps in CO_2 methanation to the gas-generation rate was less than in the case of Ni (211). The purpose in this study was to investigate the effects of applying a direct electric field and co-adsorbed oxygen atoms; these effects could be evaluated on any Ni facet. Therefore, we used the Ni (111) surface in the first step owing to the simplicity of the calculation. In addition, seven hydrocarbon species related to the above three RDSs were used to examine the adsorption and reaction energies.
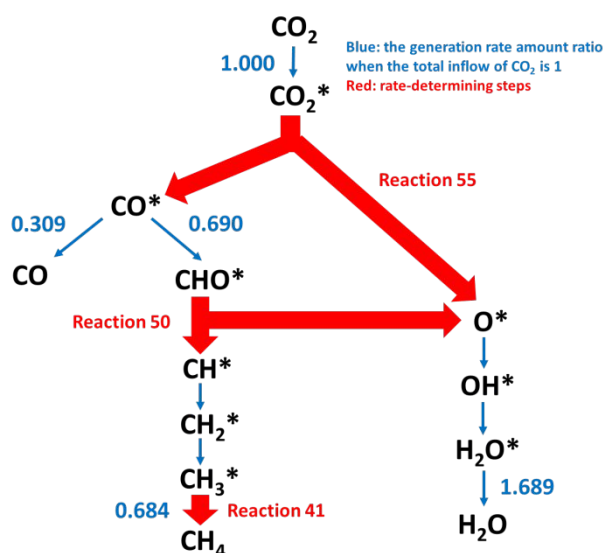

Fig. 6 Schematic of main reaction paths for CO_2 methanation on the Ni (211) surface.

Direct effects of surface-adsorbed species with an electric field

We performed first-principles calculations to investigate the effect of the direct change in catalytic electron state with an applied electric field in NEMCA on CO_2 methanation, using the thin-film condenser model.

First, we calculated the adsorption energies of seven hydrocarbon species on the Ni (111) facet related to RDSs during CO_2 methanation. The changes in the adsorption energy of each species upon varying the electric field are shown in Table 2 and Fig. 7. The adsorption energies under an electric field are listed in Table S4. These results show that the direct effects of the electric field on surface adsorption differ for each

species. In Table 2 and Fig. 7, the negative values indicate the adsorption stabilization of the adsorbed species. H atoms, O atoms, and CO have a positive linear relationship; CH and CH_3 exhibit a negative linear relationship; and CO_2 and CHO have a semi-harmonic relationship. Here, O atoms, CH, and CO are considered as examples. The O atom was stabilized by the electric field in the [0 0 –1] direction, whereas the CH atom was stabilized by the electric field in the [0 0 1] direction.

Normally, electric charges flow from the Ni-metal surface to the adsorbed species by back-donation to stabilize surface adsorption. In the case of a monoatomic species such as an O atom, the O atom is negatively charged, and the Ni atoms are positively charged by back-donation for O adsorption on the Ni metal surface, inducing an electric dipole moment between the O and Ni atoms, as shown in Fig. 8. Therefore, when an electric field in [0 0 1] is induced on the Ni-metal surface, the adsorption stability decreases toward the direction opposite to that of the electric field in [0 0 1], as expressed in Eq. 17. In addition, according to Mulliken charge analysis, the inflow amount of charges (i.e., the number of electrons) from the Ni-metal surface to the adsorbed O atom by back-donation decreases with the electric field in [0 0 1], as shown in Table S5.

$$U = -\boldsymbol{d} \cdot \boldsymbol{E} \ [17]$$

where U is the dipole moment energy, $\boldsymbol{d}$ is the electric dipole moment, and $\boldsymbol{E}$ is the external electric field. In addition, according to Eq. 18, atomic polarization is induced in the O atom exposed to an external electric field, and the adsorption stability increases with the electric field in [0 0 1] along the same induced electric dipole moment direction as the electric field in [0 0 1], as shown in Fig. 8.

$$\boldsymbol{p} = \alpha \boldsymbol{E} \ [18]$$

where $\boldsymbol{p}$ is the electric dipole moment induced by atomic polarization, and α is the atomic (effective) polarizability. However, the effect of the induced polarization was considered to be small. Hence, the strength of the bond between the O atom and the Ni-metal surface decreases with the electric field in the [0 0 1] direction. The direct electric field effect for other monoatomic species can be explained using the same mechanism.

In the case of a polyatomic species such as CH, CH is polarized for surface adsorption and has an electric dipole moment in the direction from the C atom to the H atom. This indicates that the adsorption stability increases with the electric field in [0 0 1] along the same electric dipole moment direction as the electric field in [0 0 1], as shown in Fig. 8. Consequently, the strength of the bond between CH and the Ni-metal surface increased. CO, another polyatomic species, is also polarized for surface adsorption and has an electric dipole moment along the direction from the O atom to the C atom, unlike CH. This implies that the adsorption stability decreases with the electric field in [0 0 1] along the electric dipole moment direction opposite to the electric field in [0 0 1], as shown in Fig. 8. Consequently, the strength of the bond between CH and the Ni-metal surface

decreased. Notably, the effect of the electric dipole moment in the adsorbed molecules was larger than the effect of the electric dipole moment between the directly adsorbed species and Ni atoms. Because the charge difference between atoms in the molecule is larger than that between the directly adsorbed O atom and three-fold Ni atoms, as shown in Table S6, the stabilization tendencies of the polyatomic species when an external electric field is applied can be attributed to the effect of the electric dipole moment in the adsorbed molecules .

Although CO_2 is stabilized by the electric field in both directions, the magnitude of stabilization imparted by the electric field in the [0 0 −1] direction is larger than in the [0 0 1] direction according to the above mechanism, which is also the case for the other polyatomic species. CO_2 is physically adsorbed onto the Ni metal surface; therefore, we infer that the semi-harmonic tendency of CO_2 is induced by its physisorption. Similarly, although CHO is stabilized by the electric field in both directions, the magnitude of stabilization with the electric field in the [0 0 1] direction is larger than in the [0 0 −1] direction according to the above mechanism, which is also the case for the other polyatomic species. CHO polarizes in both the perpendicular and horizontal directions, and we infer that CHO's semiharmonic tendency is induced by the effect of polarization (electric dipole moment) in two directions. The overall magnitude of the electric dipole moment in CHO is larger in the [0 0 1] direction of the electric field for the charge magnitude difference between each atom in CHO (such that CHO is better stabilized by the electric field in [0 0 1]).

In addition, using a direct electric field, strong stabilization effects were achieved for the CO (and O) atoms and CH_3 in the [0 0 −1] and [0 0 1] directions, respectively. This is because the change in the amount of charge (i.e., the number of electrons) by varying the external electric field is large.

Table 2. Relative value based on the adsorption energy in the absence of an electric field.

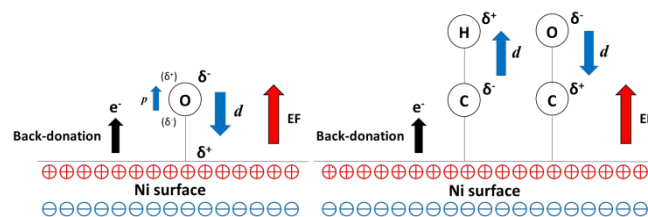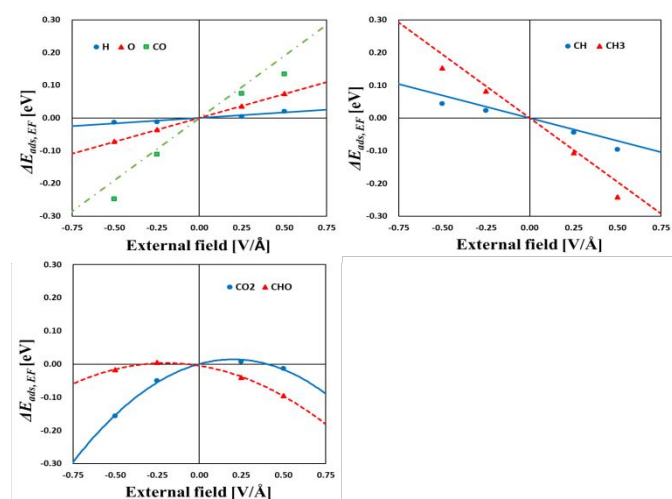| External field [V/Å]	$\Delta E_{ads,EF}$ [eV]						
	H	O	CH	CO	CH_3	CO_2	CHO
0.50	0.02	0.07	-0.10	0.13	-0.24	-0.01	-0.10
0.25	0.00	0.04	-0.04	0.07	-0.11	0.01	-0.04
-0.25	-0.01	-0.04	0.02	-0.11	0.08	-0.05	0.00
-0.50	-0.01	-0.07	0.04	-0.25	0.15	-0.16	-0.02

Fig. 7 Linear and semi-harmonic tendencies of the adsorption energy when an electric field is applied.

Fig. 8 Schematics of the electric polarization, induced (atomic) electric dipole moment, and electric dipole moment of the O atom (left side) and CH and CO species (right side) when the electric field is in the [0 0 1] direction (**p**: induced (atomic) electric dipole moment, **d**: electric dipole moment).

To validate our calculations, we compared our results to those of previous studies. Wang and Liu computed the S atoms on the Ni (100) and Ni (111) facets in the presence of an external electric field using DFT. They reported that the adsorption energy between the S atom and Ni surface is stabilized by the electric field in both directions, i.e., [0 0 ±1]. The $\Delta E_{ads,EF}$ of the S atom with an electric field strength of −0.5 V/Å is −0.19 eV.[50] In our calculation, the adsorption energy of the S atom is also stabilized by the electric field in both directions. The $\Delta E_{ads,EF}$ of the S atom for an external electric field strength of −0.5 V/Å (−0.06 eV; with the adsorbed *fcc* site as the most stable site[50,81]; see Tables S4 and S7) is in good agreement with their report, although the calculated absolute value differs from theirs because the calculation conditions are different. Therefore, stabilization by the electric field in the [0 0 ±1] directions is characteristic of the S atom. Using DFT, Mukherjee and Linic also computed the absorption energies of the H atom, O atom, and OH on the Ni (111) facet as a function of the electric field strength. They reported that the direct effects of an electric field on the surface adsorption of O atoms and OH differ. The adsorption energies of the O and OH atoms were stabilized and destabilized, respectively, by the electric field in the [0 0 −1] direction. The $\Delta E_{ads,EF}$ of the O atom and OH with an electric field strength of −0.5 V/Å are approximately −0.015 eV and 0.2 eV, respectively. They also reported that the electric field had little effect on the adsorption energy of the H atom.[51] According to our results, the O and OH species were stabilized and destabilized by the electric field in the [0 0 −1] direction, respectively, in the same manner as in their report. The $\Delta E_{ads,EF}$ of the O atom and OH (0.23 eV; the adsorbed *fcc* site was the most stable site[42,68,69,71]; see Tables S4 and S7) for an electric field strength of −0.5 V/Å are in good agreement, although the calculated absolute value differs from theirs because the calculation conditions were different. In addition, the electric field had little effect on the adsorption energy of the H atoms in our calculations. Che et al. calculated the H atom, C atom, and CH, CH_2, and CH_3 species on the Ni (111) surface in the presence of an external electric field with a strength in the range −1.0 to 1.0 V/Å.[52] They reported that the $\Delta E_{ads,EF}$ values of the C atom and CH_3, for an electric field strength of −0.5 V/Å, were

approximately –0.011 eV and 0.105 eV, respectively. We found that the C atom and CH$_3$ species are also stabilized and destabilized by the electric field in the [0 0 –1] direction, respectively, in accordance with their findings. The $\Delta E_{ads,EF}$ values of the C atom (–0.07 eV; the adsorbed *hcp* site is the most stable site[52,70,71]; see Tables S4 and S7) and the CH$_3$ species in the presence of a –0.5 V/Å electric field are in good agreement, although the calculated absolute value differs from theirs because the calculation conditions were different. They also reported that the electric field effect toward the H atom adsorption energy was considerably small, as also observed by Mukherjee and Linic[51] and us. These comparisons indicate that our calculation results are reasonable.

Direct effects of surface reactions with an electric field

We also studied the surface reaction energy of each RDS during CO$_2$ methanation under a direct electric field. Table 3 lists the surface reaction energy changes for each RDS under a direct electric field. The surface reaction energies in the presence of the electric field are listed in Table S8. Notably, the surface reaction energy decreased owing to the electric field from the gas phase to the Ni metal surface in the [0 0 –1] direction in all RDSs. We have discussed the reason for this from the viewpoint of the change in adsorption energy with application of a direct electric field. For the CHO* and CO$_2$* dissociations, stabilization of the bond between the O* atom and CO* on each product side and the Ni-metal surface occurs when the electric field is in the [0 0 –1] direction. For CH$_4$ desorption, the bond between CH$_3$* and the Ni-metal surface destabilizes when the electric field is in the [0 0 –1] direction, which simplifies CH$_4$ desorption to the gas phase. Hence, the equilibrium in all RDSs leans toward the product side owing to the electric field in the [0 0 –1] direction. From these observations, the overall CO$_2$ methanation is promoted by the electric field in the [0 0 –1] direction. These trends are also applicable to other reactions. The Boudouard reaction (2CO = CO$_2$ + C [19]) and cracking reaction, which are well known to occur in carbon deposition at high solid-oxide fuel cell (SOFC) operating temperatures, are examples.[82–103] The Boudouard reaction, which uses CO as a reactant, may be restrained by an electric field in the [0 0 –1] direction because the equilibrium in this reaction leans toward the reactant side owing to the stabilization of CO adsorption. The cracking reaction generated CH$_x$-type species on the product side as the reaction progressed. It is speculated that the adsorption of CH$_x$-type species is destabilized by the electric field in the [0 0 –1] direction; thus, the cracking reaction may be restrained by the electric field in the [0 0 –1] direction because the equilibrium in this reaction leans toward the reactant side.

Table 3 Relative values based on the surface reaction energy in the absence of an electric field.

External field [V/Å]	$\Delta E_{rxn,EF}$ [eV]		
	CHO* + * → CH* + O*	CO$_2$* + * → CO* + O*	CH$_3$* + H* → CH$_4$ + 2*
0.50	0.07	0.23	0.22
0.25	0.02	0.10	0.10
-0.25	-0.01	-0.10	-0.07
-0.50	0.00	-0.16	-0.14

Moreover, a detailed kinetic simulation was performed, and the calculated overall CH$_4$ generation rate revealed the promotion and suppression of the overall CO$_2$ methanation via the direct electric field effect on the RDSs. Kinetic and thermodynamic parameters involving an activation barrier parameter on Ni (211) and (100) were also required for our detailed kinetic simulation, although the DFT calculations were performed for only the (111) facet. In our kinetic simulation, we assumed that the effects of the direct electric field induction only on the activation barrier parameters and that the effects of the direct electric field on the activation barrier parameters on the Ni (211) and (100) facets are identical to those on the Ni (111) facet. Furthermore, we used reaction energy differences with and without an electric field to simulate the effect of the direct electric field on the activation barrier parameter in our kinetic simulations. In other words, we added the DFT reaction-energy changes on Ni (111): $\Delta E_{rxn,EF}$ to the activation-barrier parameters for the three RDSs on Ni (111), (211), and (100) in our kinetic simulation to evaluate the direct electric field effect on the overall CO$_2$ methanation. More detailed information on the parameter change is shown in Table S9; the overall CH$_4$ generation rate under each electric field magnitude (0, ±0.25, and ±0.5 V/Å) is shown in Fig. 9. This figure shows that the CH$_4$ generation rate increased as the electric field strength increased in the [0 0 –1] direction, whereas it decreased as the electric field increased in the [0 0 1] direction. In the solid-oxide electrolysis cell (SOEC) mode, the electric current flows from the anode to the cathode, which means that electrons move in this direction. An electric field is induced from the electrolyte to the Ni-metal surface under these conditions. This indicates that
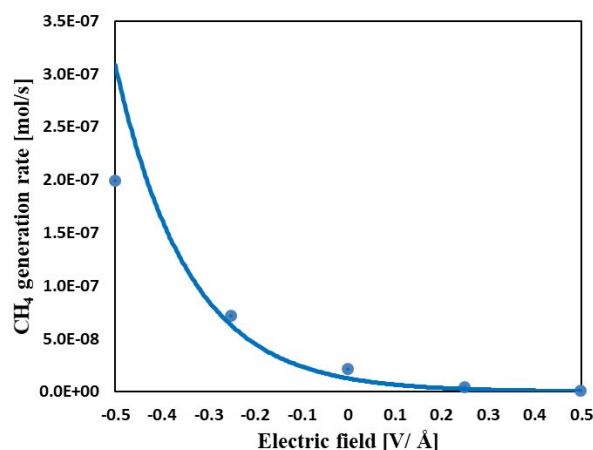
overall CO$_2$ methanation was promoted in the SOEC mode.
Fig. 9 Overall CH$_4$ generation rate for electric field magnitudes of 0, ±0.25, and ±0.5 V/Å.

Effects of surface-adsorbed species with co-adsorbed oxygen atoms

We used first-principles calculations to evaluate the spillover effects of a lattice (co-adsorbed) oxygen anion toward the catalyst surface with an electric field in NEMCA for CO$_2$ methanation, considering the co-adsorbed oxygen atom surface model.

First, we calculated the adsorption energy of hydrocarbon species on Ni (111) related to the RDSs during CO_2 methanation with co-adsorbed oxygen atoms. Table 4 shows the changes in the adsorption energy of each species with the co-adsorbed oxygen atoms. The absolute adsorption energies for the co-adsorbed oxygen atoms are also listed in Table S10. This table shows that the adsorption energy of all adsorbed species increases as the co-adsorbed oxygen atom coverage increases and indicates that all hydrocarbon species are less stable owing to a steric barrier effect in the presence of co-adsorbed oxygen atoms. However, the relationship between the adsorption energy change and the oxygen-atom coverage is not linear, and the destabilization effect for ϑ = 1/6 and 1/4 is larger than for ϑ = 2/9. The dependence of the oxygen coverage on the adsorption energies of the O atom and CO is shown in Fig. 10. In the presence of co-adsorbed oxygen atoms on the *fcc* site, the adsorbed hydrocarbon species adsorbed only on confined *fcc* or *hcp* sites, as shown in Fig. 3. Accordingly, the distance between the co-adsorbed oxygen atoms and the adsorbed hydrocarbon species for ϑ = 1/6 and 1/4 are closer than for ϑ = 2/9, so the steric barrier effect is larger. This indicates that the destabilization of species adsorption with co-adsorbed oxygen atoms does not depend on the oxygen-atom coverage but on the distance between the co-adsorbed oxygen atoms and the adsorbed hydrocarbon species to produce a steric barrier effect.

We compared our calculation results for the co-adsorbed oxygen atoms and application of a direct electric field with those of other studies. Liu et al. performed DFT calculations with H atoms, O atoms, OH, and H_2O on Ni (111) as a function of co-adsorbed oxygen-atom coverage. They reported that the binding energies between the H atom, O atom, and the Ni surface decreased with increasing co-adsorbed oxygen-atom coverage. The relative value based on the binding energies of H and O atoms without co-adsorbed oxygen atoms for ϑ = 2/9 are 0.08 eV and 0.21 eV, respectively[42]. In our calculations, the adsorption energies between the H atom, O atom, and the Ni surface decreased with increasing co-adsorbed oxygen-atom coverage, which is the same trend found in the previous report. The $\Delta E_{ads,co-ad\,O}$ of the H atom for ϑ = 2/9 is in good agreement with their report. Although the $\Delta E_{ads,co-ad\,O}$ of the O atom for ϑ = 2/9 is slightly different from their result, this difference is assumed to arise from a calculation error because the adsorption energy of the O atom is large (−5.12 eV). This comparison indicates that our DFT calculations are reasonable.

Table 4 Relative values based on the adsorption energy without co-adsorbed oxygen atoms.

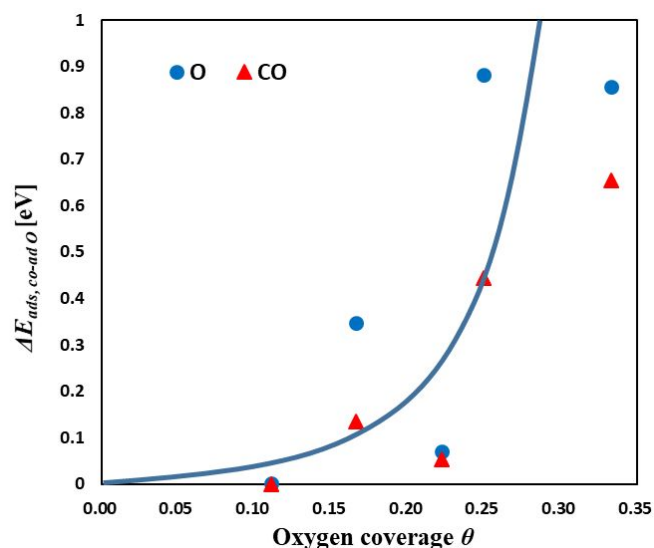| O co-adsorption coverage: θ	$\Delta E_{ads,co-ad\,O}$ [eV]						
	H	**O**	**CH**	**CO**	**CH$_3$**	**CO$_2$**	**CHO**
θ=1/9	0.01	0.00	0.02	-0.01	-0.05	-0.05	-0.03
θ=1/6	0.07	0.35	0.22	0.13	-0.13	-0.04	0.14
θ=2/9	0.05	0.07	0.06	0.05	-0.02	-0.03	-0.05
θ=1/4	0.17	0.88	0.53	0.44	0.44	0.00	0.78
θ=3/9	0.23	0.86	0.75	0.65	0.85	-0.02	0.79

Fig. 10 Oxygen-coverage dependence on the adsorption energy of the O atom and CO.

Effects of surface reactions with co-adsorbed oxygen atoms

The surface reaction energy of each RDS during CO_2 methanation with the co-adsorbed oxygen atoms was then calculated (Table 6). The surface reaction energies for the co-adsorbed oxygen atoms are also listed in Table S11. This table shows the different trends in the surface reaction energies for each RDS during CO_2 methanation. It can be seen that the surface reaction energy for CHO and CO_2 dissociation increased, whereas that for CH_4 desorption decreased with increasing co-adsorbed oxygen-atom coverage. These tendencies were caused by the destabilization of the adsorption energy as the co-adsorbed oxygen-atom coverage increased. For ϑ = 1/9 and 2/9, the interaction between the adsorbed species and the Ni-metal surface is weaker owing to the existence of co-adsorbed oxygen atoms. However, for ϑ = 3/9, the steric barrier effect when co-adsorbed oxygen atoms are present is large. During the CHO and CO_2 dissociations, the number of species on the reaction surface increases from one to two, and an O* atom is generated on the product side as the reaction proceeds. During CH_4 desorption, the number of species on the reaction surface decreases from two to zero as the reaction proceeds. Hence, the equilibrium in CHO and CO_2 dissociation leans toward the reactant side, whereas the equilibrium in CH_4 desorption leans toward the product side.

Table 5 Relative value based on surface reaction energies in the absence of co-adsorbed oxygen atoms.

O co-adsorption coverage: θ	$\Delta E_{rxn,co-ad\,O}$ [eV]		
	CHO* + * $\rightarrow$ CH* + O*	**CO$_2$* + * $\rightarrow$ CO* + O***	**CH$_3$* + H* $\rightarrow$ CH$_4$ + 2***
θ=1/9	0.05	0.03	0.04
θ=1/6	0.43	0.52	0.03
θ=2/9	0.18	0.15	-0.03
θ=1/4	0.61	1.30	-0.90
θ=3/9	0.81	1.53	-1.08

Subsequently, we calculated the activation energy of each RDS for CO_2 methanation with co-adsorbed oxygen atoms using a TS search for close examination because the surface reaction energies in the RDS follow different trends, as shown in Table 5 (the configurations of the initial step, transition state, and final step geometries for CHO dissociation, CO_2 dissociation, and CH_4 desorption on the Ni (111) facet under oxygen-atom coverage for ϑ = 1/9 are shown in Fig. S2 as an example). Table 6 shows the activation energy of each RDS for ϑ = 0, 1/9, and 2/9. This result indicates that the activation energies of the RDSs with co-adsorbed oxygen atoms follow the same trend as the surface reaction energy. In summary, the activation barriers of CHO and CO_2 dissociation increased, and the activation barrier of CH_4 desorption decreased as the co-adsorbed oxygen-atom coverage increased.

Table 6 Activation energy changes when co-adsorbed oxygen atoms are present.

O co-adsorption coverage: θ	$E_{act,co\text{-}ad\ O}$ [eV]		
	CHO* + * → CH* + O*	CO_2* + * → CO* + O*	CH_3* + H* → CH_4 + 2*
θ=0	1.09	0.63	1.02
θ=1/9	1.29	0.80	0.51
θ=2/9	1.53	0.80	0.34

Furthermore, a detailed kinetic simulation was performed, and the overall CH_4 generation rate was calculated to identify the promotional and restraint effects involved in the overall CO_2 methanation by the co-adsorbed oxygen atoms on the RDSs. In addition to the direct electric-field induction, kinetic and thermodynamic parameters involving an activation barrier parameter on Ni (211) and (100) were also required to perform our kinetic simulations, although DFT calculations were performed only for the (111) facet. In our kinetic simulation, we assumed that the effects of oxygen-atom co-adsorption only affect the activation barrier parameters, and that the effects of oxygen atom co-adsorption on the activation barrier parameters on the Ni (211) and (100) facets are the same as those on the Ni (111) facet. Moreover, we used the activation energy differences for the scenarios with and without co-adsorbed oxygen-atom coverage to simulate the effect of oxygen-atom co-adsorption on the activation barrier parameters, i.e., we added DFT activation-energy changes on Ni (111): $\Delta E_{act,co-ad\ O}$ to the activation barrier parameters in the three RDSs on Ni (111), (211), and (100) to evaluate the spillover effect of lattice oxygen on the overall CO_2 methanation. More detailed information on the parameter changes is given in Table S12; the overall CH_4 generation rate for oxygen-atom coverages of ϑ = 0, 1/9, and 2/9 is shown in Fig. 11, which indicates that the CH_4 generation rate decreased with increasing oxygen-atom coverage. In the SOEC mode, oxygen anions flow from the cathode to the anode via the electrolyte, decreasing the oxygen-atom coverage on the Ni-metal surface. This result reveals that the overall CO_2 methanation is accelerated in the SOEC mode.
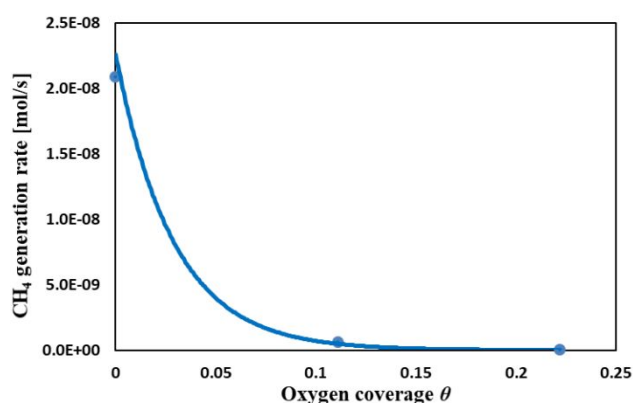

Fig. 11 Overall CH_4 generation rate for oxygen-atom coverages of ϑ = 0, 1/9 and 2/9.

Discussions on our calculation under practical operation conditions

Finally, we compared both the direct electric-field induction and co-adsorbed oxygen effects, which were discussed above, and determined the dominant factor in the NEMCA mechanism over CO_2 methanation based on practical SOC system conditions.

The DFT calculation results with a direct electric-field induction and co-adsorbed oxygen atoms in this study are under extreme conditions because our research purpose was to propose the trends of kinetic energy change with a direct electric field or co-adsorbed oxygen atoms. In realistic SOCs, the electric potential is the potential difference that a charge experiences when ions (O^{2-}) in the electrolyte exchange electrons (e^-) with the Ni catalyst via electrochemical reactions. However, our simulation uses a thin-film condenser model with a direct electric field between the Ni catalyst surface and the vacuum layer, so our model cannot be directly compared with practical systems. Thus, we estimated the magnitude of the electric field in a practical model using the effective electrolyte thickness to compare the magnitude of the electric field applied to our model with that in practical systems. The electric potential strength between the anode and cathode regions in practical SOC is approximately the range from 0.5 to 1.0 V, and the effective thickness of the electrolyte is ≈1 μm,[104] which assumes that the practical electric potential difference ranges from 0.5 to 1.0 V/μm. In this study, our DFT calculation involving a direct electric field was performed for field strengths of 0, ±0.25, and ±0.5 V/Å. Therefore, if our result has a linear relationship to the practical calculation, we should only multiply our calculated values by ≈10^{-4} in order to compare our DFT calculation with the practical conditions. Meanwhile, co-adsorbed oxygen-atom coverage with the working voltage of 0.5 V is approximately ϑ = 0.01 in the practical condition estimated using our simulation. Our DFT calculation with co-adsorbed oxygen atoms in this study was performed using a co-adsorbed oxygen-atom coverage of ϑ = 0, 1/9, 1/6, 2/9, 1/4, or 3/9. Therefore, if our result is linearly related to the practical calculation, we only have to multiply our calculation values by approximately 10^{-1} to compare our DFT calculation with the

practical condition, which is the same as the direct electric field calculation. For example, with this information in mind, approximately compared with our reaction energy results for a direct electric field strength of 0.5 V/Å and co-adsorbed oxygen-atom coverage of $\vartheta = 1/9$, the spillover effects of a lattice oxygen toward the catalyst surface may be larger than the direct change in the catalytic electron state with an electric field in NEMCA during CO_2 methanation.

Conclusions

We first performed a sensitivity analysis and detailed kinetic simulation of the CO_2 methanation reaction paths on the Ni (211), (111), and (100) surfaces to determine the RDSs and main reaction paths involved in CO_2 methanation. These simulations indicate that the (211) facets have the highest sensitivity to the gas-generation rate and that CHO* dissociation, CO_2* dissociation, and CH_4 desorption are the RDSs in CO_2 methanation. In addition, the sensitivity of the Ni (111) facet was identical to that of the Ni (211) facet, although it was smaller than that of Ni (211). Subsequently, we performed DFT calculations to study the electric field effect on the catalytic activity by comparing the calculated properties of hydrocarbon species (i.e., adsorption, surface reaction, and activation energies) with and without direct electric field induction or co-adsorbed oxygen atoms on a Ni (111) catalyst surface. The adsorption energy of each hydrocarbon species on the Ni (111) facet associated with the RDSs in CO_2 methanation exhibited a different trend, and the reaction energies in all RDSs decreased with the application of an electric field. These results indicate that a direct electric field enhances the stability of the adsorbed species on the catalyst surface and accelerates all the RDSs. In addition, a detailed kinetic simulation was conducted, which revealed the promotional and restraint effects of a direct electric field on the overall CO_2 methanation. Our detailed kinetic simulations showed that the overall CH_4 generation rate is accelerated by the electric field from the gas phase to the Ni-metal surface, while it is decelerated by the electric field from the Ni-metal surface to the gas phase. Furthermore, overall CO_2 methanation is accelerated in the SOEC mode. As the number of co-adsorbed oxygen atoms increased, the adsorption energies of the hydrocarbon species on the Ni (111) facet associated with the RDSs in CO_2 methanation increased. However, the destabilization tendency is nonlinear with respect to the co-adsorbed oxygen-atom coverage because the distance between some adsorbed species when $\vartheta = 1/6$ and 1/4 is closer than when $\vartheta = 2/9$ on account of an adsorption site restriction. In addition, the reaction and activation energies in the CO_2 and CHO dissociations increased, while CH_4 desorption decreased. These results indicate that the steric barrier effect of the co-adsorbed oxygen atoms restrained the stability of the adsorbed species on the catalyst surface. The detailed kinetic simulation revealed the promotional and restraint effects of co-adsorbed oxygen atoms on the overall CO_2 methanation. The overall CH_4 generation rate decelerated as the oxygen coverage increased, and that of the overall CO_2 methanation was accelerated in the SOEC mode. It is difficult to identify an interrelation between

the magnitude of the electric field and the co-adsorbed oxygen-atom coverage by comparing the direct effect of the electric field with the effect of co-adsorbed oxygen atoms; however, the spillover effect of lattice oxygen toward the catalyst surface may be larger than the direct change in the catalytic electron state with an electric field. We believe that our research on the theoretical mechanism of NENCA will facilitate the development of more energetically effective catalytic technologies and help to overcome serious energy issues. These findings will hopefully garner attention from the research community regarding the probability of applying NEMCA to catalytic technologies.

As a next step, we will examine the relationship between the magnitude of the electric field and co-adsorbed oxygen-atom coverage more closely to determine the adaptability and quantitativity of our results to catalytic improvements with an electric field under practical SOC conditions. Moreover, the calculation of the effect of a direct electric field under more realistic conditions will be planned using another DFT method: the effective screening medium (ESM) method.[54,59,105–111] Our present results with co-adsorbed oxygen atoms are insufficient to explain the NEMCA mechanism involved in CO_2 methanation in a practical SOC system. The coverage of the co-adsorbed oxygen atoms on the step sites may be large owing to the large adsorption energy, and the effect of the co-adsorbed oxygen atoms on the step sites may be more localized because the steric effect is large for short distances between the adsorbed atoms. Therefore, DFT calculations with co-adsorbed oxygen atoms on step sites, such as Ni (211), are also being used to obtain more active effects that can explain the NEMCA mechanism in CO_2 methanation with a practical SOC system.[53,70,72,73,81,112–117]

Conflicts of interest

There are no conflicts of interest to declare.

Acknowledgements

References

1   T. Yamaguchi, H. Shimada, U. Honda, H. Kishimoto, T. Ishiyama and Y. Fujishiro, *ECS Trans.*, 2015, **68**, 3459.
2   R. Atsumi, T. Ishiyama, H. Kishimoto, D.B. Katherine, K. Yamaji, T. Yamaguchi and Y. Fujishiro, *J. Fuel Cell Tech.*, 2016, **16**, 76. written in Japanese
3   K. Wakamatsu and T. Ogura, *ECS Trans.*, 2019, **91**, 2613.

4   K. P. Kuhl, T. Hatsukade, E. R. Cave, D. N. Adram, J. Kibsgaard and T. F. Jaramillo, *J. Am. Chem. Soc.*, 2014 **136**, 14107.

5   J. Ducamp, A. Bengaouer and P. Baurens, *Can. J. Chem. Eng.*, 2017, **95**, 241.

6   M. Ni, *Can. Int. J. Hydrog. Energy*, 2012, **37**, 6389.

7   C. Fukuhara, S. Ratchahat, Y. Suzuki, M. Sudoh and R. Watanabe, *Chem. Lett.*, 2018, **48**, 196.

8   C. Fukuhara, S. Ratchahat, A. Kamiyama, M. Sudoh and R. Watanabe, *Chem. Lett.*, 2019, **48**, 441.

9   K. Manthiram, B. J. Beberwyck and A. P. Alivisatos, *J. M. Chem. Soc.*, 2014, **136**, 13319.

10 L. Torrebte-Murciano, D. Mattia, M. D. Jones and P. K. Plucinski, *J. CO$_2$ Util.*, 2014, **6**, 34.

11 C. G. Vayenas, S. Bebelis, C. Pliangos, S. Brosda and D. Tsiplakides, Electrochemical activation of catalysis: promotion, Electrochemical Promotion and Metal–Support Interactions, Kluwer Academic/Plenum Publishers, New York, 2001.

12 R. Imbihl, *Prog. Surf. Sci.*, 2010, **85**, 241.

13 P. Vernoux and C. G. Vayenas, *Prog. Surf. Sci.*, 2011, **86**, 83.

14 D. R. Lambert, in: A. Wieckowski, E. Savinova and C.G. Vayenas (Eds.), Catalysis and Electrocatalysis at Nanoparticles Surfaces, Marcel Dekker, New York, 2003.

15 G. L. Haller, *J. Catal.*, 2003, **216**, 12.

16 C. G. Vayenas and C. G. Koutsodontis, *J. Chem. Phys.*, 2008, **128**, 182506.

17 D. Tsiplakides and S. Balomenou, *Catal. Today*, 2009, **146**, 312.

18 A. Katsaounis, *J. Appl. Electrochem.*, 2010, **40**, 885.

19 C. G. Vayenas, *J. Solid State Electrochem.*, 2011, **15**, 1425.

20 P. Vernoux, L. Lizarraga, A. De Lucas-Consuegra, J. L. Valverde, S. Souentie, C. Vayenas, D. Tsiplakides, S. Balomenou and E. A. Baranova, *Chem. Rev.*, 2013, **113**, 8192.

21 C. G. Vayenas, *Catal. Lett.*, 2013, **143**, 1085.

22 Y. Sekine, M. Haraguchi, M. Matsukata and E. Kikuchi, *Catal. Today*, 2011, **171**, 116.

23 K. Oshima, T. Shinagawa and Y. Sekine, *J. Jpn. Petrol. Inst.*, 2013, **56**, 11.

24 M. Stoukides and C. G. Vayenas, *J. Catal.*, **70**, 137 (1981).

25 C. G. Vayenas, S. Brosda and C. Pliangos, *J. Catal.*, 2003, **216**, 487.

26 S. G. Neophytides and C. G. Vayenas, *Ionics*, 1995, **1**, 80.

27 B. Xing and G. C. Wang, *Phys. Chem. Chem. Phys.*, 2014, **16**, 2621.

28 F. Dorado, A. de Lucas-Consuegra, P. Vernoux and J. L. Valverde, *Appl. Catal. B*, 2007, **73**, 42.

29 C. G. Vayenas and S. I. Bebelis, *Solid State Ion.*, 1997, **94**, 267.

30 I. V. Yentekakis, G. Moggridge, C. G. Vayenas and R. M. Lambert, *J. Catal.*, 1994, **146**, 292.

31 M. Marwood and C. G. Vayenas, *J. Catal.*, 1998, **178**, 429.

32 S. Wodiunig and C. Comninellis, *J. European Ceram. Soc.*, 1999, **19**, 931.

33 J. Poppe, S. Volkening, A. Schaak, E. Schutz, J. Janek and R. Imbihl, *Phys. Chem. Chem. Phys.*, 1999, **1**, 5241.

34 A. Toghan, L. M. RÖsken and R. Imbihl, *ChemPhysChem*, 2010, **11**, 1452.

35 R. M. Lambert, F. J. Williams, A. Palermo and M. S. Tikhov, *Top. Catal.*, 2000, **13**, 91.

36 S. Ladas, S, Kennou, S, Bebelis and C. G. Vayenas, *J. Phys. Chem.*, 1993, **97**, 8845.

37 S. G. Neophytides and C. G. Vayanas, *J. Phys. Chem.*, 1995, **99**, 17063.

38 E. Mutoro, B. Luerssen, S. Guenther and J. Janek, *Solid State Ion.*, 2009, **180**, 1019.

39 E. P. M. Leiva, C. V*á*zquez, M. I. Rojas and M. M. Mariscal, *J. Appl. Electrochem.*, 2008, **38**, 1065.

40 I. S. Fragkopoulos, I. Bonis and C. Theodoropoulos, *Chem. Eng. Sci.*, 2013, **104**, 647.

41 I. S. Fragkopoulos and C. Theodoropoulos, *Electrochimica. Acta.*, 2014, **150**, 232.

42 S. Liu, T. Isimoto and M. Koyama, *Appl. Surf. Sci.*, 2015, **333**, 86.

43 G. C. Wang, S. X. Tao and X. H. Bu, *J. Catal.*, 2006, **244**, 10.

44 I. S. Metcalfe, *J. Catal.*, 2001, **199**, 247.

45 C. G. Vayenas and G. E. Pitselis, *Ind. Eng. Chem. Res.*, 2001, **40**, 4209.

46 D. Presvytes and C. G. Vayenas, *Ionics*, 2007, **13**, 9.

47 G. Foti, V. Stankovic, I. Bolzonella and C. Comninellis, *J. Electroanal. Chem.*, 2002, **532**, 191.

48 I. Bonis, S. Valiño-Pazos, I. S. Fragkopoulos and C. Theodoropoulos, *Comput. Aided Chem. Eng.*, 2011, **29**, 151.

49 J. S. Chinchilla, K. Asazawa, T. Sakamoto, K. Yamada, H. Tanaka and P. Strasser, *J. Am. Chem. Soc.*, 2011, **133**, 5425.

50 J. H. Wang and M. Liu, *Electrochem. Commun.*, 2007, **9**, 2212.

51 J. Mukherjee and S. Linic, *J. Electrochem. Soc.*, 2007, **154**, B919.

52 F. Che, R. Zhang, A. J. Hensley, S. Ha and J. S. McEwen, *Phys. Chem. Chem. Phys.*, 2014, **16**, 2399.

53 F. Che, A. J. Hensley, S. Ha and J. S. McEwen, *Catal. Sci. Technol.*, 2014, **4**, 4020.

54 I. Hamada and Y. Morikawa, *J. Phys. Chem. C*, 2008, **112**, 10889.

55 S. A. Wasileski, M. T. M. Koper and M. J. Weaver, *J. Am. Chem. Soc.*, 2002, **124**, 2796.

56 L. D. Chen, M. Urushihara, K. Chan and J. K. Nørskov, *ACS Catal.*, 2016, **6**, 7133.

57 M. P. Hyman and J. W. Medlin, *J. Phys. Chem. B*, 2005, **109**, 6304.

58 E. Skúlason and H. Jónsson, *Adv. Phys-X*, 2017, **2**, 481.

59 C. Freysoldt and J. Neugebauer, *Phys. Rev. B*, 2018, **97**, 205425.

60 P. Hohenberg and W. Kohn, *Phys. Rev.*, 1964, **136**, B864.

61 W. Kohn and L. J. Sham, *Phys. Rev.*, 1965, **140**, A1133.

62 R. M. Martin, Electronic Structure, Cambridge University Press, Cambridge, 2004.

63 D.R. Lide, CRC Handbook of Chemistry and Physics, CRC press, New York, 1996.

64 J. P. Perdew, K. Burke and M. Ernzerhof, *Phys. Rev. Lett.*, 1996, **77**, 3865.

65 H. J. Monkhorst and J. D. Pack, *Phys. Rev. B: Solid State*, 1976, **13**, 5188.

66 T. A. Halgren and W. N. Lipscomb, *Chem. Phys. Lett.*, 1977, **49**, 225.

67 N. Govind, M. Petersen, G. Fitzgerald, D. K. Smith and J. Andzelm, *Comput. Mater. Sci.*, 2003, **28**, 250.

68 M. Pozzo, G. Carlini, R. Rosei and D. Alfè, *J. Chem. Phys.*, 2007, **126**, 164706.

69 A. A. Phatak, W. N. Delgass, F. H. Ribeiro and W. F. Schneider, *J. Phys. C*, 2009, **113**, 7269.

70 Z. B. Ding and M. Maestri, *Ind. Eng. Chem. Res.*, 2019, **58**, 9864.

71 D. W. Blaylock, T. Ogura, W.H. Green and G. J. O. Beran, *J. Phys. Chem. C*, 2009, **113**, 4898.

72 A. D. Karmazyn, V. Fiorin, S. J. Jenkins and D. A. King, *Surf. Sci.*, 2003, **538**, 171.

73 D. W. Blaylock, Y. A. Zhu and W. H. Green, *Top Catal.*, 2011, **54**, 828.

74 T. Ogura, Y. Shiratori, T. Shiraga, H. Tsukikawa and M. Tajima, *Proc. of IMPRES*, 2013, **4**, 9.

75 Y. Shiratori, T. Ogura, H. Nakajima, M. Sakamoto, Y. Takahashi, Y. Wakita, T. Kitaoka and K. Sasaki, *Int. J. Hydrogen Energy*, 2013, **38**, 10542.

76 T. Ogura, *Catal.*, 2015, **57**, 499. written in Japanese

77 T. Ogura, *J. Combus. Soc. Japan*, 2018, **60**, 260. written in Japanese

78   L. F. Shampine and M. W. Reichelt, *SIAM J. Sci. Comput.*, 1997, **18**, 1.

79   L. F. Shampine, M. W. Reichelt and J. A. Kierzenka, *SIAM Rev.*, 1999, **41**, 538.

80   H. Li, M. Zhaoand Q. Jiang, *J. Phys. Chem. C*, 2009, **113**, 7594.

81   C. R. B. Rodr´ıguez and J. A. Santana, *J. Chem. Phys.*, 2018, **149**, 204701.

82   A. E. Castro Luna and A. M. Becerra, *React. Kinet. Catal. Lett.*, 1997, **61**, 375.

83   J. Sehested, *Catal. Today*, 2006, **111**, 103.

84   V. Eveloy, *Appl. Energy*, 2012, **93**, 107.

85   J. N. Amor, *Appl. Catal. A: Gen.*, 1999, **176**, 159.

86   J. M. Klein, Y. Bultel, M. Pons and P. Ozil, *Trans. ASME, J. Fuel Cell Sci. Technol.*, 2007, **4**, 425.

87   Y. Cui, H. Zhang, H. Xu and W. Li, *Appl. Catal. A: Gen.*, 2007, **318**, 79.

88   J. M. Ginsburg, J. Piña, T. El Solh and H. I. de Lasa, *Ind. Eng. Chem. Res.*, 2005, **44**, 4846.

89   J. R. Rostrup-Nielsen and J. H. Bak Hansen, *J. Catal.*, 1993, **144**, 38.

90   S. Wang and G. Q. Lu, *Energy Fuels*, 1996, **10**, 896.

91   M. C. J. Bradford and M. A. Vannice, *Appl. Catal. A: Gen.*, 1996, **142**, 73.

92   L. Pinaeva, Y. Schuurman and C. Mirodatos, Carbon Routes in Carbon Dioxide Reforming of Methane: Environmental Challenges and Greenhouse Gas Control for Fossil Fuel Utilization in the 21st Century, Kluwer Academic/Plenum Publishers, New York, 2002.

93   U. Olsbye, O. Moen, A. Slagtern and J. M. Dahl, *Appl. Catal. A: Gen.*, 2002, **228**, 289.

94   B. S. Liu and C. T. Au, *Appl. Catal. A: Gen.*, 2003, **244**, 18.

95   D. Pakhare and J. Spivey, *Cem. Soc. Rev.*, 2014, **43**, 7813.

96   D. Singh, , E. Hernández-Pacheco, P. N. Hutton, N. Patel, and M. D. Mann, *J. Power Sources*, 2005, **142**, 194.

97   P. Chen, Z. Hou, X. Zheng and T. Yashima, *React. Kinet. Catal. Lett.*, 2005, **86**, 51.

98   K. Girona, J. Laurencin, J. Fouletier and F. Letebvre-Joud, *J. Power Sources*, 2012, **210**, 381.

99   K. Girona, J. Toyir, P. Gélin, and Y. Bultel, *ECS Trans.*, 2011, **35**, 945.

100   A. Lanzini and P. Leone, *Int. J. Hydrog. Energy*, 2010, **35**, 2463.

101   C. Xu, J. W. Zondlo, M. Gong, F. Elizalde-Blancas, X. Liu and I. B. Celik, *J. Power Sources*, 2010, **195**, 4583.

102   Y. Shiratori, T. Ijichi, T. Oshima and K. Sasaki, *Int. J. Hydrog. Energy*, 2010, **35**, 7905.

103   H. S. Bengaard, J. K. Nørskov, J. Sehested, B. S. Clausen, L. P. Nielsen, A. M. Molenbroek and J. R. Rostrup-Nielsen, J. Catal., 2011, **209**, 365.

104   H. Watanabe, A. Unemoto, K. Amezawa and T. Kawada, *ECS Trans.*, 2009, **25**, 1939.

105   M. Otani and O. Sugino, *Phys. Rev. B*, **73**, 115407 (2006).

106   M. Otani, *J. Vac. Soe. Jpn.*, 2011, **54**, 512. written in Japanese

107   I. Hamada, O. Sugino, N. Bonnnet and M. Otani, *Phys. Rev. B*, 2013, **88**, 115427.

108   N. Bonnnet, T. Morishita, O. Sugino and M. Otani, *Phys. Rev. Lett.*, 2012, **109**, 266101.

109   S. Nishihara and M. Otani, *Phys. Rev. B*, 2017, **96**, 115429.

110   M. Otani, I. Hamada, O. Sugino, Y. Morikawa, Y. Okamoto and T. Ikeshoji, *J. Phys. Soc. Jpn.*, 2008, **77**, 024802-1.

111   S. Nishihara and M. Otani, *Phys. Rev. B*, 2017, **96**, 115429.

112   D. B. Cao, Y. W. Li, J. Wang and H. Jiao, *Surf. Sci.*, **603**, 2991 (2009).

113   K. Yang, M. Zhang and Y. Yu, *Phys. Chem. Chem. Phys.*, 2015, **17**, 29616.

114   J. X. Liu, B. Y. Zhang, P. P Chen, H. Y. Su and W. X. Li, *J. Phys. Chem. C*, 2016, **120**, 24895.

115   H. Orita, N. Itoh and Y. Inada, *Surf. Sci.*, **571**, 161 (2004).

116   H. J. Li, A. C. Lausche, A. A. Peterson, H. A. Hansen, F. Studt and T. Bligaard, *Surf. Sci.*, 2015, **641**, 105.

117   T. R. Munter, T. Bligaard, C. H. Christensen and J. K. Nørskov, *Phys. Chem. Chem. Phys.*, 2008, **10**, 5202.